

# Toward Durable Protonic Ceramic Cells: Hydration-Induced Chemical Expansion Correlates with Symmetry in the Y-Doped BaZrO<sub>3</sub>–BaCeO<sub>3</sub> Solid Solution

Ting Chen,<sup>◆</sup> Yuhang Jing,<sup>◆</sup> Lawrence O. Anderson,<sup>◆</sup> Kwati Leonard,<sup>◆</sup> Hiroshige Matsumoto, Narayana Aluru, and Nicola H. Perry\*



Cite This: *J. Phys. Chem. C* 2021, 125, 26216–26228



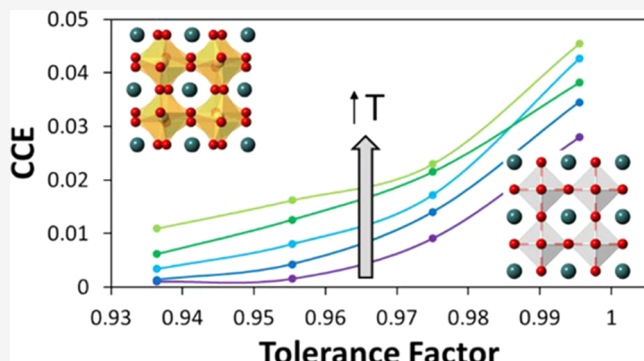
Read Online

## ACCESS |

Metrics & More

Article Recommendations

**ABSTRACT:** Electrolytes and electrodes in protonic ceramic electrolysis/fuel cells (PCECs/PCFCs) can exhibit significant chemical strains upon incorporating H<sub>2</sub>O into the lattice. To increase PCEC/PCFC durability, oxides with lower hydration coefficients of chemical expansion (CCEs) are desired. We hypothesized that lowering symmetry in perovskite-structured proton conductors would lower their CCEs and thus systematically varied the tolerance factor through B-site substitution in the prototypical BaCe<sub>0.9-x</sub>Zr<sub>x</sub>Y<sub>0.1</sub>O<sub>3-δ</sub> (0 ≤ x ≤ 0.9) solid solution. X-ray diffraction (XRD) confirmed that symmetry decreased with decreasing Zr content. CCEs were measured by isothermal XRD, dilatometry, and thermogravimetric analysis (TGA) in varied pH<sub>2</sub>O over 430–630 °C. With decreasing Zr content, the isothermal H<sub>2</sub>O uptake was greater, but the corresponding chemical strains were smaller; therefore, CCEs monotonically decreased. Density functional theory simulations on end-member BaCe<sub>1-y</sub>Y<sub>y</sub>O<sub>3-δ</sub> and BaZr<sub>1-y</sub>Y<sub>y</sub>O<sub>3-δ</sub> compositions showed the same trend. Lower CCEs in this solid solution correlate to decreasing symmetry, increasing unit cell volume, increasing oxygen vacancy radius, decreasing bulk modulus, and inter- vs intraoctahedral hydrogen bonding. Microstructural constraints may also contribute to lower macroscopic CCEs in lower-symmetry bulk ceramics based on the observed anisotropic chemical expansion and enhanced strains in powder vs bulk BaCe<sub>0.9</sub>Y<sub>0.1</sub>O<sub>3-δ</sub>. The results inform design principles for the rational tailoring of CCEs and materials choice for chemomechanically durable devices.



## 1. INTRODUCTION

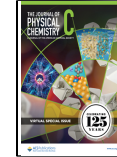
Electrochemical devices, such as fuel/electrolysis cells, are integral components of a sustainable energy infrastructure.<sup>1,2</sup> Fuel cells can efficiently derive electrical power and heat from air and a variety of fuels, while their reverse operation as electrolysis cells provides a means to store electrical energy as chemical fuel. Typically, solid oxide fuel/electrolysis cells operate at high temperatures (600–1000 °C), while proton-exchange membrane or polymer electrolyte membrane cells operate at low temperatures (25–100 °C). Bridging these two typical temperature ranges to work in the intermediate-temperature range (~400–600 °C) has the potential to combine some of the benefits of both low- and high-temperature operations—high efficiency, no precious-metal catalysts, and fuel flexibility (high temperature) plus short start-up times, low-cost interconnect materials, and high durability (low temperature). To operate solid oxide cells at intermediate temperatures, materials with high ionic conductivity and low electronic conductivity are needed for the electrolyte layer. Certain proton-conducting oxides offer higher

ionic conductivity<sup>3–5</sup> than the best oxide ion conductors (acceptor-stabilized ZrO<sub>2</sub>, acceptor-doped CeO<sub>2</sub>, and Sr- and Mg-codoped LaGaO<sub>3</sub>) and so can operate at lower temperatures with the same Ohmic resistance for an equivalent electrolyte geometry. Additionally, electrolysis cells using proton-conducting electrolytes generate H<sub>2</sub> at the fuel electrode that is undiluted with H<sub>2</sub>O, and proton conductors are also under development for gas separation and electrochemical reactors.<sup>5–9</sup> Among proton conductors, the Y-doped BaZrO<sub>3</sub>–BaCeO<sub>3</sub> solid solution has received significant attention. The wide-band-gap zirconate end member offers high ionic conductivity and stability but is challenging to sinter

**Received:** September 21, 2021

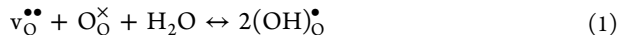
**Revised:** November 8, 2021

**Published:** November 18, 2021

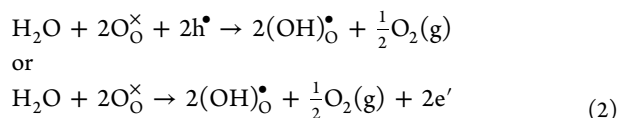


to full density leading to high grain boundary electrical resistance,<sup>10–12</sup> while the cerate end member offers greater ease in processing, higher proton content at elevated temperatures, and lower hole transference numbers<sup>13</sup> but with less tolerance for humid, CO<sub>2</sub>-containing environments<sup>14</sup> and higher n-type electronic conductivity under reducing conditions.<sup>15,16</sup> Intermediate compositions provide a compromise between the strengths and weaknesses of the end members, with BaZr<sub>0.7</sub>Ce<sub>0.2</sub>Y<sub>0.1</sub>O<sub>3-δ</sub> being a composition of choice in some studies.<sup>17,18</sup>

In addition to transporting protons through the lattice, these acceptor-doped materials can also exchange H<sub>2</sub>O with the surrounding gas environment, as described in eq 1



Here, water from the gas phase dissociates as it enters the ceramic lattice, filling an oxygen vacancy and inserting H species. The O and H ions are often denoted as effectively sharing an oxygen site via the (OH)<sub>O</sub><sup>•</sup> Kroger–Vink notation. Reaction 1 is valid for operation in a condition where concurrent redox reactions, enabling the hydrogenation processes<sup>19–22</sup> shown in eq 2, are deemed insignificant, e.g., due to the negligible concentration of electronic defects in the measurement conditions relative to oxygen vacancies. (The first hydrogenation process is for a p-type system, while the hypothetical second reaction is for an n-type system, which is not typically reported in this context.)



The pure hydration process in eq 1, which is studied in the present work, is accompanied by a distortion in the lattice, termed chemical strain or chemical expansion, with significant implications for device mechanical integrity. Phenomenologically, the linear chemical strain ( $\epsilon_C$ ) is often found to be proportional to the change in defect concentration ( $\Delta[(OH)_O^\bullet]$  for the hydration reaction, with units of concentration per formula unit) by the linear coefficient of chemical expansion (CCE), as shown in eq 3

$$CCE = \frac{\epsilon_C}{\Delta[(OH)_O^\bullet]} \quad (3)$$

Macroscopically, in randomly oriented polycrystalline materials, the scalar treatment of the CCE is appropriate. At an atomistic scale, simulations have represented chemical expansion by point defect-induced strain tensors with locally anisotropic behavior possible even in nominally cubic systems.<sup>23,24</sup> In noncubic systems, anisotropic strains can be observed on a single-crystal or local grain level.<sup>25–27</sup> In such cases, the volumetric chemical expansivity would be the sum of the linear CCEs along the three orthogonal directions. The chemical stress associated with all of these chemical strains can be large enough to cause mechanical failure such as cracking and delamination within devices where components are constrained and/or experiencing nonuniform defect concentrations.<sup>28,29</sup> This effect can be particularly pronounced in proton conductors, compared to oxygen loss in mixed oxide ion and electronic conductors, as hydration-induced lattice strains of up to 1% have been reported.<sup>30,31</sup> Therefore, there is interest in quantifying CCEs for the purposes of device design and modeling as well as in understanding chemical and

structural design rules for rationally tailoring CCEs to optimize the components' chemomechanical response.

Several groups have reported observations of hydration-induced chemical expansion in acceptor-doped BaZrO<sub>3</sub>–BaCeO<sub>3</sub>.<sup>32–35</sup> Computationally, density functional theory (DFT) simulations have modeled the size and shape of point defects involved in the hydration process, as in eq 1. Jedvik et al. have shown that oxygen vacancies ( $v_O^{\bullet\bullet}$ ) are smaller than (OH)<sub>O</sub><sup>•</sup> defects, which are smaller than oxide ions O<sub>O</sub><sup>X</sup>. In this case, the chemical expansion process may be a competition between a slight contraction induced by replacing O<sub>O</sub><sup>X</sup> with (OH)<sub>O</sub><sup>•</sup> and a larger expansion induced by replacing  $v_O^{\bullet\bullet}$  with (OH)<sub>O</sub><sup>•</sup>. Experimentally, with the exception of a macroscopic study by Kreuer using dilatometry,<sup>1</sup> most papers on proton conductors report chemical strains at the unit cell level measured by *in situ* X-ray or neutron diffraction.<sup>30,31,36,37</sup> Although diffraction enables insight into strain anisotropy, the common nonisothermal methodology has not lent itself well to accurate, quantitative determination of hydration CCEs. Typically, lattice parameters vs temperature are measured while heating and cooling,<sup>31,37,38</sup> during which process the hydration degree varies, leading to deviations from conventional thermal expansion behavior; i.e., the total strain is a superposition of thermal and chemical contributions. If the measurements are performed in a single gas atmosphere, i.e., one humidity, chemical strains at a given temperature can arise from hysteresis in hydration degree during heating vs cooling. In this case, the strains are measured in a nonequilibrium condition, and nonuniform proton concentrations throughout the material in such cases may result in peak broadening or asymmetry. Chemical strains can also be measured in equilibrium conditions by repeating a temperature excursion in different gas atmospheres, i.e., different H<sub>2</sub>O contents, and dwelling at each temperature point until steady-state behavior is obtained. It should be noted that these variable-temperature approaches typically assume that the thermal expansion contribution is constant, regardless of hydration degree; however, a recent study has shown that (iso-stoichiometric) coefficients of thermal expansion are hydration-dependent.<sup>34</sup> This means that hysteretic differences in strain during heating vs cooling, or equilibrium strain differences in different humidities, may be attributable to changes in thermal strain as well as chemical strain, even though they have been attributed to solely chemical strain in previous studies. Such nonisothermal measurements also assume that redox processes during heating and cooling are negligible,<sup>39</sup> which may not be the case, depending on the oxygen partial pressure and temperature. In the present work, we instead pursue an isothermal approach that enables the isolation of chemical strain from any thermal effects, in equilibrium (uniform proton concentration), absent of significant redox contributions.

To determine CCEs, the changes in proton concentration must be measured under identical conditions to the measured chemical strains. Therefore, isothermal comparisons in different humidities (keeping the oxygen partial pressure constant at an intermediate value) are preferred. Generally, such direct comparisons of strain and quantified proton content change have not yet been made in the literature for all of these compositions. Reported hydration-induced chemical strains for this solid solution (typically in the temperature range 300–600 °C) range from 0.03<sup>40</sup> to 0.5%<sup>32</sup> and, for Y-doped BaZrO<sub>3</sub>, increase with increasing acceptor dopant concentration, as expected from eq 1, because the change in proton

concentration can be greater when more oxygen vacancies are stabilized in the structure. The Reported CCEs for this solid solution range over an order of magnitude with values as low as 0.006,<sup>40</sup> but often, the changes in proton concentration were assumed to represent full hydration/dehydration, rather than measured, likely leading to some CCE underestimations. Even in the rare cases with the proton concentration change measured at isolated temperature points, there is considerable variation,<sup>41</sup> with reported CCEs varying by a factor of 5 for BaCeO<sub>3</sub> materials<sup>31,42</sup> (~0.01–0.05 CCE estimated from volumetric chemical expansivity) and by at least a factor of 2 for BaZrO<sub>3</sub> materials<sup>32</sup> (~0.045–0.09 CCE estimated from volumetric chemical expansivity) depending on the Y content.

In this work, we seek to provide macroscopic CCE values over a range of practical application temperatures by measuring isothermal chemical strains by dilatometry and XRD and associated isothermal proton concentration changes by thermogravimetric analysis (TGA) under identical partial pressures of H<sub>2</sub>O and ensuring attainment of steady-state conditions. Further, by studying four compositions systematically across the solid solution, by both *in situ* characterization and density functional theory simulation, we aim to uncover and understand, on a structural and chemical basis, the trends in CCE. Our initial hypothesis was that perovskite proton conductors with increasing crystallographic distortions (lower symmetry) vs cubic perovskites would exhibit decreasing CCEs. In this solid solution, we can systematically vary the A:B-site average cation size ratio to induce crystallographic distortions leading to different symmetries, as predicted by a tolerance factor analysis. At a crystal chemical level, we consider that distorted perovskites may accommodate chemical stresses through facile changes in their octahedral tilts/rotations; such changes would lengthen some bonds and shorten others, so that one expects only small overall lattice volume changes. As a result of the reduced symmetry (vs cubic perovskites), we expect that distorted perovskites will exhibit anisotropic chemical expansion, as has been observed before for other compositions.<sup>25,27,43–45</sup> At a macroscopic level, in polycrystalline bulk ceramics with randomly oriented grains, this anisotropy may lead to (a) averaging of linear chemical strains in any given direction and (b) constraining of the strain from adjacent grains—both effects potentially lowering CCEs in addition to any crystal chemical effects. The latter effect (b) would be less apparent in unconstrained powders. In the description that follows, we present our experimental and computational results, clarifying the CCE trend in the cerate-zirconate solid solution and its correlation to various structural features including symmetry.

## 2. APPROACH

**2.1. Experimental Approach.** **2.1.1. Fabrication.** Powders of BaZr<sub>0.9</sub>Y<sub>0.1</sub>O<sub>3-δ</sub> ( $x = 0.9$ ), BaZr<sub>0.6</sub>Ce<sub>0.3</sub>Y<sub>0.1</sub>O<sub>3-δ</sub> ( $x = 0.6$ ), BaZr<sub>0.3</sub>Ce<sub>0.6</sub>Y<sub>0.1</sub>O<sub>3-δ</sub> ( $x = 0.3$ ), and BaCe<sub>0.9</sub>Y<sub>0.1</sub>O<sub>3-δ</sub> ( $x = 0$ ) were synthesized by a modified chemical solution route as described elsewhere<sup>46</sup> using analytic-grade metal nitrates—Ba(NO<sub>3</sub>)<sub>2</sub> (Wako, 99.9%), ZrO(NO<sub>3</sub>)<sub>2</sub> (Sigma-Aldrich, 99%), Ce(NO<sub>3</sub>)<sub>3</sub>·6H<sub>2</sub>O (Kanto Chemical Co., INC 99.99%), and Y(NO<sub>3</sub>)<sub>3</sub>·6H<sub>2</sub>O (Mitsuwa's Pure Chemicals, 99.9%)—as raw materials. Stock solutions of the metal nitrates with concentrations determined by an inductively coupled plasma technique (ICP Shimadzu, ICPE-9000) were weighed and added into an aqueous solution sequentially with continuous stirring. Ethylenediamine tetraacetic acid (EDTA) (Dojindo,

99%) and citric acid (Wako, 99%) were then added as chelating agents with a molar ratio of the total metal ions to EDTA and citric acid set at 1:1.5:1.5. Ammonium hydroxide solution (Chameleon Regent, 28.0% NH<sub>3</sub> in H<sub>2</sub>O) was added to promote the dissolution of EDTA and to adjust the pH to ~9. The solution was then heated under stirring to evaporate water until it changed into a viscous gel. The gel was then heat-treated at 240 °C in a vacuum oven to obtain a solid precursor, which was calcined at 900 °C for 10 h in air. The resulting powder was roll-milled for 4 days to produce uniform, submicrometer particles, which were dried. The obtained powders were pelletized with a Newton press and further compressed by cold isostatic pressing at 250 MPa. The compressed pellets were then sintered at 1400–1550 °C (higher temperature for Zr-rich samples) for 10 h. Bars (~22.5 mm × ~4 mm × ~3.5 mm) were cut from pellets using a diamond saw.

**2.1.2. Characterization.** Phase purity of the synthesized pellets was initially confirmed by X-ray diffraction (XRD Ultima IV) with Cu K $\alpha$  radiation (40 kV, 40 mA). Diffraction patterns were obtained at room temperature in the 2 $\theta$  range between 10 and 80° with a step size of 0.02°. Space group symmetry and lattice parameters were analyzed by pattern matching (PDFs 01-070-6747, 04-018-2314, 04-008-4455, and 04-020-2236 for  $x = 0, 0.3, 0.6$ , and  $0.9$ , respectively) and Rietveld refinement using HighScore software (Panalytical). Relative densities were estimated from geometric and mass measurements of dried samples. Tolerance factors were calculated using Shannon's ionic radii<sup>47</sup> from eq 4,<sup>48</sup> where  $r_A$ ,  $r_B$ , and  $r_X$  are the A-site, B-site, and anion radii, respectively

$$t = \frac{r_A + r_X}{\sqrt{2}(r_B + r_X)} \quad (4)$$

Ionic radii values used were 1.61 Å (Ba<sup>2+</sup> XII-fold-coordinated), 0.9 Å (Y<sup>3+</sup> VI), 0.72 Å (Zr<sup>4+</sup> VI), 0.87 Å (Ce<sup>4+</sup> VI), and 1.4 Å (O<sup>2-</sup> VI).

Dilatometry was performed on the bar-shaped specimens using a lab-assembled single pushrod dilatometer to measure the expansion upon increasing the steam content in a pure N<sub>2</sub> gas atmosphere at various temperatures in the range of 430–630 °C. Temperature was held constant in each case while the humidity was stepped to different values, and each humidity condition was held until the sample had reached a steady-state length. N<sub>2</sub> was selected to avoid high hole concentrations,<sup>49,50</sup> which could be present in more oxidizing conditions, given the acceptor doping; similarly, highly reducing conditions were avoided to minimize the presence of Ce<sup>3+</sup>; these constraints were chosen to limit the presence of the redox reactions shown in eq 2.<sup>49</sup> The steam content or pH<sub>2</sub>O was controlled at 1.06% by bubbling the N<sub>2</sub> through water at 8 °C, with temperature controlled by a water bath (Multi Circulator MCX-250, AS ONE, Japan). No significant expansion was observed when the pH<sub>2</sub>O was changed from ~1 to 20% at different values; therefore, the pH<sub>2</sub>O change from ~0% (UHP N<sub>2</sub> gas that has bypassed the water bath) to 1.06% was selected in this work. The corresponding isothermal changes of proton concentration ( $\Delta[(OH)_0^\bullet]$ ) were measured by thermogravimetric analysis (TGA, lab-assembled, using a Mettler-Toledo XP6 microbalance) under the same conditions as the dilatometry measurement by evaluating the mass changes according to eq 5

$$\Delta[(\text{OH})_0^\bullet] = \frac{\Delta m / \text{MW}_{\text{OH}}}{m_i / \text{MW}_{\text{BCZY}}} \quad (5)$$

where  $\Delta m$  is the isothermal mass change from  $\sim 0$  to 1.06%  $\text{pH}_2\text{O}$ ,  $m_i$  is the initial (dry) mass, and  $\text{MW}_x$  is the molecular weight of  $x$ . The  $\text{pH}_2\text{O}$  was also controlled by bubbling  $\text{N}_2$  through water, with temperature controlled by a water bath. Owing to the possibility of sample mechanical failure during testing, which could influence dilatometric results, samples were analyzed by optical microscopy to check for the presence of any microcracks after the *in situ* characterization. Additionally, several replicates of the  $x = 0$  composition were tested with varying porosities, and in all cases, repeat measurements for hydration and dehydration in each condition were performed to check reversibility in both the TGA and dilatometry measurements.

To observe the crystal structure as a function of temperature and humidity, to compare bulk vs powder hydration strains and to observe chemical strain anisotropy, *in situ*, high-temperature XRD (HTXRD) was performed on the least-symmetric (lowest tolerance factor)  $\text{BaCe}_{0.9}\text{Y}_{0.1}\text{O}_{3-\delta}$  end member. HTXRD was performed using a Bruker D8 Advance (Model #D8 Advance A25) with an Anton Paar HTK 1200N nonambient stage and a Dectris Eiger2R\_500K detector, using  $\text{Cu K}\alpha$  radiation with line focus, 60 mm Göbbel mirror, and 0.2 mm divergence slit primary optics. A thermocouple in contact with the bottom of the sample stage monitored the sample temperature. In the temperature range where hydration is expected, i.e., 430–630 °C, scans were taken with a 0.01° step size and 0.5 seconds/step over the  $2\theta$  range 25–90°. For all other temperatures, the scan rate was increased to 0.25 seconds/step. Scans were performed under the same conditions as the dilatometry and TGA measurements, except for the order of measurement: a series was first run in dry  $\text{N}_2$ , and then the measurements were repeated in  $\text{N}_2$  with 1.06%  $\text{H}_2\text{O}$ . The powder sample was held at each temperature for 90 min prior to the XRD scan, and the measurements were made from high- to low-temperature steps in each case. Data were analyzed using pattern matching to ICSD structure files for  $\text{BaCe}_{0.9}\text{Y}_{0.1}\text{O}_{3-\delta}$  (*Pnma* #165828, *Imma* #193052, and *R\bar{3}c* #193056) and Rietveld refinement with TOPAS (Bruker AXS, Version 6) software. Refinement parameters were added in the following sequence: fourth-order Chebychev polynomial background, the appropriate structure file (lattice parameters), microstrain, sample displacement correction, and surface roughness correction. Near phase transitions, each structure file was fit individually, then together, to determine the contributions from each phase.  $R_{wp}$  values were less than 10% for all sample conditions.

**2.2. Computational Approach.** Density functional theory (DFT) calculations were performed with the projector-augmented wave (PAW) method,<sup>51</sup> as implemented in the Vienna ab initio simulation package (VASP).<sup>51–53</sup> The Perdew–Burke–Ernzerhof (PBE)<sup>54</sup> exchange–correlation functional was used. The cutoff energy for the plane-wave basis set was 500 eV for all calculations. For improved accuracy, the pseudopotentials with valence states of Ba (5s, 5p, 6s), Zr (4s, 4p, 5s, 4d), Ce (5s, 5p, 6s, 5d, 4f), Y (4s, 4p, 5s, 4d), and O (2s, 2p) are chosen for all calculations. All atoms were relaxed by a conjugate gradient method until the forces on each atom were less than 0.02 eV/Å.

The orthorhombic bulk  $\text{BaCeO}_3$  unit cell and cubic bulk  $\text{BaZrO}_3$  unit cell were optimized using  $6 \times 6 \times 4$  and  $6 \times 6 \times 6$

Monkhorst–Pack  $k$ -point meshes, respectively. The obtained lattice constants of the orthorhombic  $\text{BaCeO}_3$  unit cell ( $a = 6.25$  Å,  $b = 6.26$  Å,  $c = 8.85$  Å) and cubic  $\text{BaZrO}_3$  unit cell ( $a = 4.22$  Å) are in good agreement with previous DFT and experimental results.<sup>55,56</sup> Based on the optimized unit cell, a  $\text{BaCeO}_3$  supercell with  $2 \times 2 \times 2$  orthorhombic unit cells and a  $\text{BaZrO}_3$  supercell with  $3 \times 3 \times 3$  cubic unit cells were constructed and optimized. Next, one oxide ion vacancy was introduced in the supercells with two Zr or Ce ions substituted by two Y ions. The preferred positions of these two Y ions and the oxide ion vacancy were obtained by comparing the total energies of the system while locating them at different atomic sites. Finally, bulk Y-doped  $\text{BaCeO}_3$  (BCY) and Y-doped  $\text{BaZrO}_3$  (BZY) were obtained. A  $2 \times 2 \times 2$  Monkhorst–Pack  $k$ -point mesh was used for bulk calculations of BCY and BZY.

### 3. RESULTS

**3.1. Experimental.** Relative densities of the sintered samples were found to be  $68 \pm 6\%$ . The densities were intentionally kept below 100% to facilitate faster kinetics of hydration/dehydration and attainment of equilibrium in each condition studied by TGA and dilatometry. (The hydration/dehydration kinetics in dense samples are expected to be limited by oxygen diffusion,<sup>57,58</sup> which can be sluggish in the temperature range of this study.) This porosity could contribute to fracture during chemical expansion measurements,<sup>59,60</sup> but postanalysis microscopy did not reveal the presence of cracks in the majority of samples. The  $x = 0.6$  sample exhibited some surface microcracks after analysis. One  $x = 0$  sample broke during measurement and was not included in the analysis. Room-temperature X-ray diffraction patterns of as-prepared samples are shown in Figure 1. Figure 1a shows the full range of  $2\theta$  values, confirming the perovskite structure

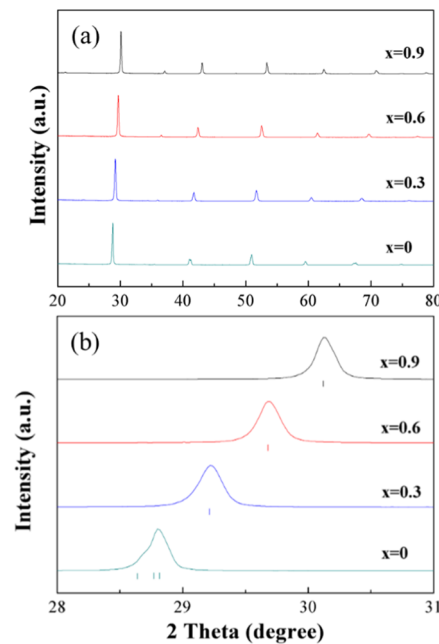


**Figure 1.** Room-temperature X-ray diffraction patterns of the four compositions showing perovskite phase peaks (a) and a selection of the data (b) showing positional shift and distortion of the most intense peak as Zr content ( $x$ ) decreases. Indices from left to right are *Pnma* (green): 200, 002, 121; *R\bar{3}c* (blue and red): 110, 104; and *Pm\bar{3}m* (black): 110.

**Table 1.** Selected Measured Properties for  $\text{BaCe}_{0.9-x}\text{Zr}_x\text{Y}_{0.1}\text{O}_{3-\delta}$  and Calculated Properties of  $\text{BaCe}_{1-y}\text{Y}_y\text{O}_{3-\delta}$  and  $\text{BaZr}_{1-y}\text{Y}_y\text{O}_{3-\delta}$ <sup>a</sup>

$x$	$t$	$a_{pc}$ at 25 °C (Å)	space group	CCE at 430 °C, measured	CCE at 630 °C, measured	CCE at 0 K, DFT
[Y] = 0.1						[Y] = 0.06–0.07
0	0.936	4.40 (4.69 DFT at 0 K)	$Pnma$	0.00098	0.019	0.01269 (0.0122)
0.3	0.955	4.33	$R\bar{3}c$	0.0015	0.019	
0.6	0.975	4.27	$R\bar{3}c$ (close to $Pm\bar{3}m$ )	0.0091	0.023	
0.9	0.996	4.21 (4.24 DFT at 0 K)	$Pm\bar{3}m$	0.028	0.049	0.02959 (0.01557)

<sup>a</sup>Note: simulated values in round parentheses are for a less stable dopant configuration with distant Y dopants rather than the more stable configuration of closely spaced Y dopants used for the majority of the data.

with no significant secondary phase contributions for each sample, while Figure 1b shows an enlarged portion of the data in the  $2\theta$  range 28–31°. Refinement of the patterns identified room-temperature space group symmetries of cubic  $Pm\bar{3}m$  for  $x = 0.9$ , rhombohedral  $R\bar{3}c$  for  $x = 0.6$  and 0.3 although  $x = 0.6$  was very close to  $Pm\bar{3}m$  symmetry, and orthorhombic  $Pnma$  for  $x = 0$ . The increasing distortion from cubic symmetry with decreasing  $x$  is consistent with the higher ionic radius of Ce vs Zr and the corresponding decreasing calculated tolerance factors (eq 1) of 0.996, 0.975, 0.955, and 0.936 for  $x = 0.9, 0.6, 0.3$ , and 0, respectively. Substitution of the larger Ce for Zr also demonstrably increased the pseudocubic lattice parameter ( $a_{pc}$ ) from 4.21 to 4.40 Å, determined from fitting the XRD data for the actual lattice parameters and then calculating the equivalent cubic cell volumes. This trend is also visible in the shifting of peaks to lower angles with increasing Ce content in Figure 1b. These structural parameters are summarized, along with results discussed below, in Table 1.

From the dilatometry and TGA measurements, samples were observed to expand and gain mass upon increasing the  $\text{H}_2\text{O}$  content in the gas phase from ~0 to 1.06% while keeping the  $\text{pO}_2$  constant around  $10^{-4}$ – $10^{-3}$  atm according to the sensor (using high-purity  $\text{N}_2$  gas). These transitions typically took place over ~50–60 min during hydration and several hours for dehydration, regardless of temperature, suggesting that the kinetics were limited by gas exchange in the large furnace tubes. Figure 2a shows the measured isothermal equilibrium chemical strain corresponding to the  $\sim 0 \rightarrow 1.06\%$   $\text{H}_2\text{O}$  change as a function of composition. Data isotherms from 430 to 630 °C in 50 °C increments are plotted. It can be observed that with increasing Zr concentration ( $x$ ), in general, the measured chemical strain increases monotonically and significantly at a given temperature. The data at 630 °C deviate slightly from this trend, with the strain minimum occurring at intermediate values of  $x$  rather than at  $x = 0$  as for the other temperatures. For low values of  $x$  ( $x = 0, 0.3$ ), the chemical strain also increases significantly with increasing temperature. For the  $x = 1$  composition, on the other hand, the chemical strain actually decreases slightly with increasing temperature, although the magnitude of that effect is not so large. The reasons for these differences will be explored in the Discussion section.

Figure 2b shows the corresponding equilibrium change in the  $(\text{OH})_0^\bullet$  concentration per formula unit determined from the isothermal measured mass changes for  $\sim 0 \rightarrow 1.06\%$   $\text{H}_2\text{O}$ , using eq 5, as a function of Zr concentration ( $x$ ). Again, the data are plotted as isotherms from 430 to 630 °C in 50 °C increments. At all but the lowest temperature, the proton concentration change in the oxide decreases with increasing Zr concentration ( $x$ ). The proton concentration change is also generally lower with increasing temperature. For the oxide

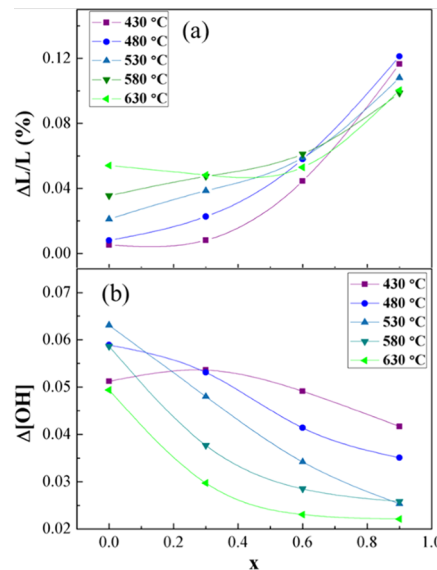


**Figure 2.** (a) Chemical strain value as a function of Zr concentration ( $x$ ) in  $\text{BaCe}_{0.9-x}\text{Zr}_x\text{Y}_{0.1}\text{O}_{3-\delta}$  and (b) the change in  $(\text{OH})_0^\bullet$  concentration per formula unit upon increasing  $\text{pH}_2\text{O}$  from ~0 to 1.06% as a function of Zr concentration ( $x$ ) in  $\text{BaCe}_{0.9-x}\text{Zr}_x\text{Y}_{0.1}\text{O}_{3-\delta}$ .

compositions in this study, the theoretical maximum change in the  $(\text{OH})_0^\bullet$  concentration that would be associated with full hydration of a dry sample would be 0.1 per formula unit based on the oxygen vacancy concentration being half that of the Y acceptor concentration and eq 1. The changes shown in Figure 2b therefore indicate that the samples are not undergoing full hydration/dehydration in these conditions. This is an important point to note, as many studies assume that full hydration and dehydration occur in estimating CCEs from XRD or dilatometric data in humid and dry conditions. As discussed in the Introduction section, such an approach could lead to underestimation of CCE values.

Figure 3a shows the CCE values derived from the data in Figure 2a,b, i.e., the chemical strain normalized to the proton concentration change per formula unit, as shown in eq 3. Data are plotted vs Zr concentration ( $x$ ) again at temperature isotherms from 430 to 630 °C. In this temperature range, the CCE increases monotonically with increasing Zr concentration ( $x$ ). This result follows clearly from the dilatometric and TGA results, as the chemical strain was generally larger for increasing  $x$ , while the mass change was generally smaller. At each composition, the CCE also increases with increasing temperature. This result again follows straightforwardly from those in Figure 2a,b, particularly as the proton concentration change decreased with increasing temperature. The CCEs (same data) are also shown as a function of temperature in Figure 3b,

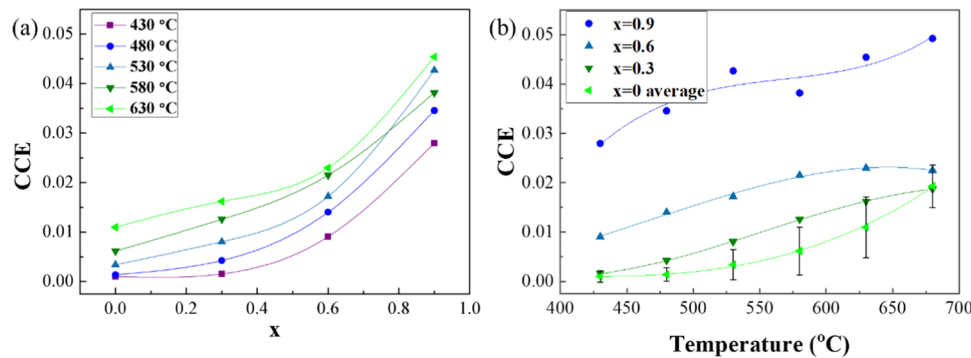


**Figure 3.** (a) CCE as a function of Zr concentration ( $x$ ) in  $\text{BaCe}_{0.9-x}\text{Zr}_x\text{Y}_{0.1}\text{O}_{3-\delta}$  and (b) CCE as a function of measuring temperature for four compositions, labeled by  $x$  in  $\text{BaCe}_{0.9-x}\text{Zr}_x\text{Y}_{0.1}\text{O}_{3-\delta}$ . The  $x = 0$  data are an average over multiple replicate samples with different densities and processing routes.

where it can clearly be seen that the magnitude of the increase in CCE with temperature is relatively similar for all of the compositions studied. Except for the  $x = 0$  composition, the temperature dependence of the CCE is roughly linear, as has been seen for perovskite compositions undergoing reduction-induced chemical expansion.<sup>61</sup> For the  $x = 0$  composition, a power law dependence is observed, as has been reported for redox-induced chemical expansion of a fluorite-structured composition.<sup>62</sup>

*In situ*, high-temperature XRD (HTXRD) was employed to determine the degree of anisotropic expansion and the effect of symmetry changes upon heating in the least-symmetric end-member,  $\text{BaCe}_{0.9}\text{Y}_{0.1}\text{O}_{3-\delta}$ . Lattice parameters from refinement are shown in Figure 4. There is a phase transition from *Pnma*

the chemical strain anisotropy at 630 °C is  $(\text{strain along } b)/(\text{strain along } a) = 2.6$  and  $(\text{strain along } b)/(\text{strain along } c) = 1.7$ .

We had initially hypothesized that this unequal expansion behavior along each axis could be a key factor in the lower observed CCEs for the lower-symmetry phases (lower  $x$ ). As mentioned, one contributing reason could be that in randomly oriented, polycrystalline sintered samples, neighboring grains with different axis alignments could constrain one another during expansion. To test this idea, the hydration strains of the  $x = 0$  composition were compared for unconstrained powder vs bulk samples. Figure 5b shows the comparison between powder HTXRD and bulk dilatometric strains. The linearized strain for the case of the anisotropically expanding powder was calculated from the cube root of the unit cell volumetric strain using the weighted average of orthorhombic and rhombohedral phase contributions. While both techniques reveal similar trends in isothermal hydration strain vs temperature, the magnitude of the strains in powder HTXRD is higher for all temperatures, suggesting that the particles in the powder are able to expand more freely, relative to the sintered bars in dilatometry. On the other hand, Figure 5b shows that powder XRD strains are greater than those in dilatometry by, at most, a factor of  $\sim 2$ , whereas CCE values of cubic  $\text{BaZr}_{0.9}\text{Y}_{0.1}\text{O}_{3-\delta}$  are greater than those of  $\text{BaCe}_{0.9}\text{Y}_{0.1}\text{O}_{3-\delta}$  by a factor of 5 or more. This large change of CCE between the zirconate and cerate end members suggests that the microstructural effect of constraining anisotropically expanding grains cannot be the only (or even primary) cause of lower CCE in the sintered Ce-containing compositions. Further, the similar and significant temperature dependence of powder XRD and bulk dilatometric isothermal chemical strain for the distorted structure of  $\text{BaCe}_{0.9}\text{Y}_{0.1}\text{O}_{3-\delta}$  suggests an important role of a common underlying crystal chemical mechanism.

HTXRD also provided observations of subtle temperature-dependent symmetry changes that may aid interpretation of the temperature dependence of the isothermal hydration strain for  $\text{BaCe}_{0.9}\text{Y}_{0.1}\text{O}_{3-\delta}$ . Although *Imma* is the dominant phase for 430–630 °C, the XRD results suggest that the structure exhibits a gradual change to higher symmetry as temperature increases within this range. This process can be seen by the convergence of  $b$  and  $c$  lattice parameters in Figure 4 and by the change in peak shape in Figure 6; two distinct peaks converge toward a single, broad peak as temperature increases, consistent with a transition from orthorhombic to rhombohedral symmetry. This observation of a gradual increase of symmetry with increasing temperature in the distorted

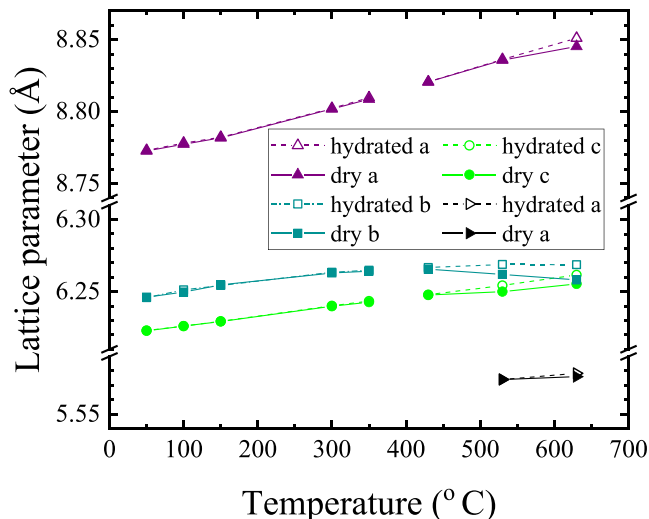


**Figure 4.** Lattice parameters for dry and hydrated  $\text{BaCe}_{0.9}\text{Y}_{0.1}\text{O}_{3-\delta}$ . Phases are *Pnma*  $\leq 350$  °C, *Imma*  $\geq 430$  °C, and contributions from  $\bar{R}\bar{3}c$   $\geq 530$  °C (black).

to *Imma* at 350 °C, and the  $\bar{R}\bar{3}c$  phase begins to contribute to the refinement at 530 °C, making up 10 and 33% of the sample at 530 and 630 °C, respectively. From the refined lattice parameters, isothermal hydration strain along each axis is shown in Figure 5a, indicating that chemical strain appears to become significant at 430 °C and above. Anisotropic expansion is clearly observed, as each axis exhibits distinguishable strain: above 430 °C, the axis-resolved isothermal hydration strain follows the order  $b > c > a$  for the *Imma* phase. Quantitatively,

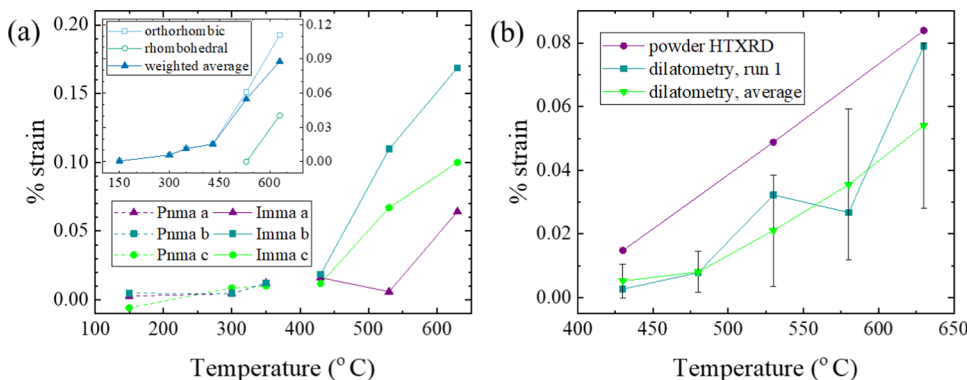


**Figure 5.** (a) Isothermal hydration-induced strain calculated from the refined lattice parameters along each axis (reference points are dry conditions at each temperature). The inset shows the linear isothermal hydration strain calculated from refined (unit cell volume)<sup>1/3</sup> changes. The weighted average includes the contribution from orthorhombic and rhombohedral phases. (b) Comparison of isothermal hydration strains measured by XRD and dilatometry for  $\text{BaCe}_{0.9}\text{Y}_{0.1}\text{O}_{3-\delta}$  (reference points are dry conditions for each temperature). The HTXRD data represent linearized average strains using a weighted average of the orthorhombic and rhombohedral phases present. “Run 1” refers to the first dilatometry sample of  $\text{BaCe}_{0.9}\text{Y}_{0.1}\text{O}_{3-\delta}$  which was also the sample run in the HTXRD measurement. “Average” refers to the average of all  $\text{BaCe}_{0.9}\text{Y}_{0.1}\text{O}_{3-\delta}$  samples tested by dilatometry. Error bars represent the standard deviations from three dilatometry experiments on different samples run under the same conditions; uncertainty in strains from the XRD measurements is smaller than the data points.

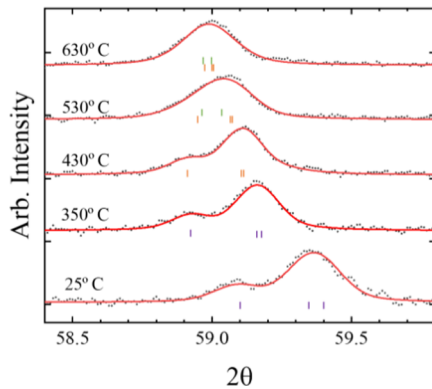


**Figure 6.** Change in peak shape illustrating the subtle move toward higher symmetry within a space group as temperature increases (*Pnma*: 25–350 °C, *Imma*: 430–630 °C). Black dots are raw data, and red lines are the Rietveld refinements.  $\text{K}\alpha_2$  contributions have been subtracted. Indices from left to right are *Pnma* (purple) and *Imma* (orange): 040, 004, 422; and  $\text{R}3\bar{c}$  (green): 422, 202.

$\text{BaCe}_{0.9}\text{Y}_{0.1}\text{O}_{3-\delta}$  composition coincides with increasing macroscopic chemical strains and CCEs with increasing temperature.

**3.2. Computational.** DFT simulations were performed to compare the structure, properties, and hydration-induced expansion behavior of the end-member  $x = 0$  (cerate) and  $x = 0.9$  (zirconate) compositions using the structural symmetries experimentally determined by XRD at 25 °C. DFT lattice parameters were in good agreement with those found experimentally, as shown in Table 1.

The obtained structures of dry BCY, hydrated BCY, dry BZY, and hydrated BZY are shown in Figure 7a–d, respectively. The dry structures contain one oxygen vacancy, while the hydrated structures contain two hydroxyl ions. Two Y dopants are close to each other, and the oxygen vacancy is located between two Y dopants for both systems in the dry state. The most stable structure of dry BZY found here is the same as that in a recent DFT result.<sup>63</sup> For the hydrated structures shown in Figure 7b,d, it is found, in both BCY and BZY systems, that the stable proton sites are in close vicinity to the dopant because of strong trapping energies with respect to the nearby Y dopant.<sup>64</sup> The proton in BCY forms hydrogen

bonds (1.78 Å; see Figure 7b) with the oxygen ions belonging to two different, neighboring octahedra (interoctahedral bonding), while the proton in BZY forms hydrogen bonds (1.65 Å; see Figure 7d) with the oxygen ions belonging to the same octahedron (intraoctahedral bonding). This difference is caused by the weaker oxygen–cerium bonds in BCY compared to stronger oxygen–zirconium bonds in BZY. The variation in bonding strength is also reflected in the bulk modulus values for these two systems, shown in Table 2, where the bulk modulus is ~33% larger for the zirconate end member.

Moreover, the hydrogen bonds are formed in hydrated BCY through octahedral rotations, as shown in Figure 7b, where one of the initial Ce–O–Y angles changes from 167.2 to 150.5°, while in hydrated BZY, the hydrogen bonds are formed by O–B–O bending motions, as shown in Figure 7d, where one of the initial O–B–O angles is reduced from 90 to 70° degrees. To further verify the simulations of the hydration reaction, we calculated the hydration enthalpy at zero pressure and zero temperature based on the total energy of each system in the Kröger–Vink hydration notation:  $\Delta E_{\text{hyd}} = E_{\text{tot}}(\text{hydrated}) - E_{\text{tot}}(V_O^{\bullet\bullet}) - E_{\text{tot}}(\text{H}_2\text{O})$ , where  $E_{\text{tot}}(\text{hydrated})$  is the total energy of the system containing two dopants and two protons,  $E_{\text{tot}}(V_O^{\bullet\bullet})$  is the total energy of the system containing two dopants and one oxide ion vacancy, and  $E_{\text{tot}}(\text{H}_2\text{O})$  is the total energy of an isolated water molecule.<sup>65,67</sup> The calculated hydration enthalpies for BCY and BZY are shown in Table 2. The hydration enthalpies are consistent with previous DFT calculations and experimental results.<sup>65,66</sup>

To address the chemical expansion, the energy as a function of volume for BCY vs hydrated BCY and BZY vs hydrated BZY was obtained, as shown in Figure 8. The data are fitted to a Birch–Murnaghan equation of state<sup>68,69</sup>

$$E(V) = E_0 + \frac{9V_0B_0}{16} \left\{ \left[ \left( \frac{V_0}{V} \right)^{2/3} - 1 \right]^3 B_0 + \left[ \left( \frac{V_0}{V} \right)^{2/3} - 1 \right]^2 \left[ 6 - 4 \left( \frac{V_0}{V} \right)^{2/3} \right] \right\} \quad (6)$$

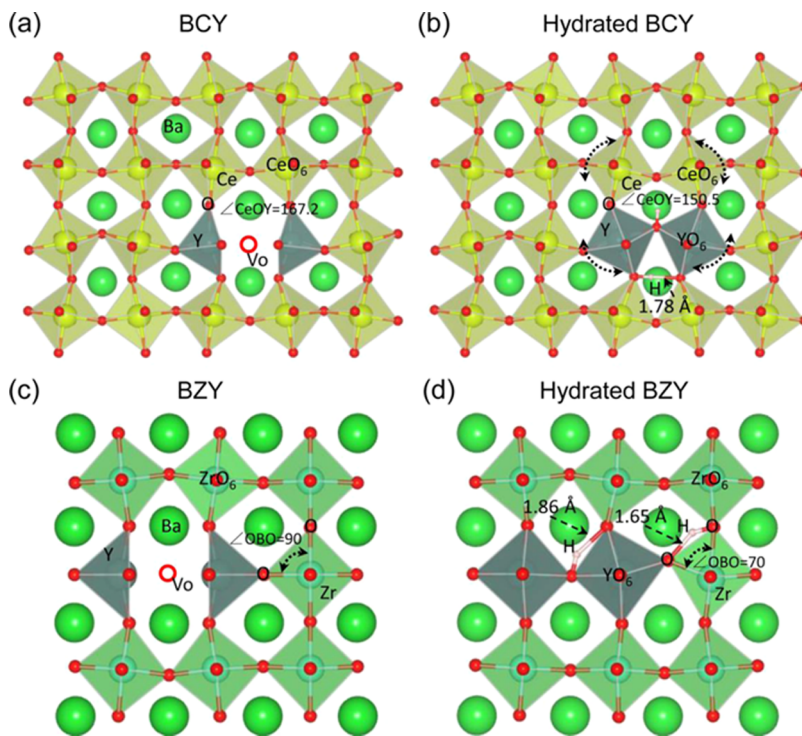


**Figure 7.** Optimized orthorhombic (a) BCY and (b) hydrated BCY systems and cubic (c) BZY and (d) hydrated BZY systems. Ba, Zr, Ce, Y, O, and H ions are green, light blue, yellow, dark blue, red, and white, respectively, and red hollow circles represent oxygen vacancies.

**Table 2. Selected Calculated Properties of  $\text{BaCe}_{1-y}\text{Y}_y\text{O}_{3-\delta}$  and  $\text{BaZr}_{1-y}\text{Y}_y\text{O}_{3-\delta}$ , with Previous Theoretical and Experimental Hydration Enthalpies Shown for Comparison<sup>a</sup>**

	$y$	$\text{BaCe}_{1-y}\text{Y}_y\text{O}_{3-\delta}$	$\text{BaZr}_{1-y}\text{Y}_y\text{O}_{3-\delta}$
hydration enthalpy (eV) GGA-PBE (this work)	0.06–0.07	-1.36 (-1.38)	-0.52 (-0.53)
hydration enthalpy (eV) GGA-PBE (Gd-BaCeO <sub>3</sub> ) <sup>55</sup>	0.06–0.07	-1.34	
hydration enthalpy (eV) experiment <sup>66</sup>	0.1	-1.68	-0.78
bulk modulus (GPa) DFT (this work)	0.06–0.07	105.9 (105.3) [dry]; 106.9 (106.8) [hydrated]	141.1 (139.1) [dry]; 140.5 (137.7) [hydrated]
Voronoi volume $v_O$ vs $O_O$ ( $\text{\AA}^3$ ), DFT (this work)	0.06–0.07	18.8 vs 18.9	14.7 vs 15.7

<sup>a</sup>Note: simulated values in round parentheses are for a less stable dopant configuration with distant Y dopants rather than the more stable configuration of closely spaced Y dopants used for the majority of the data.

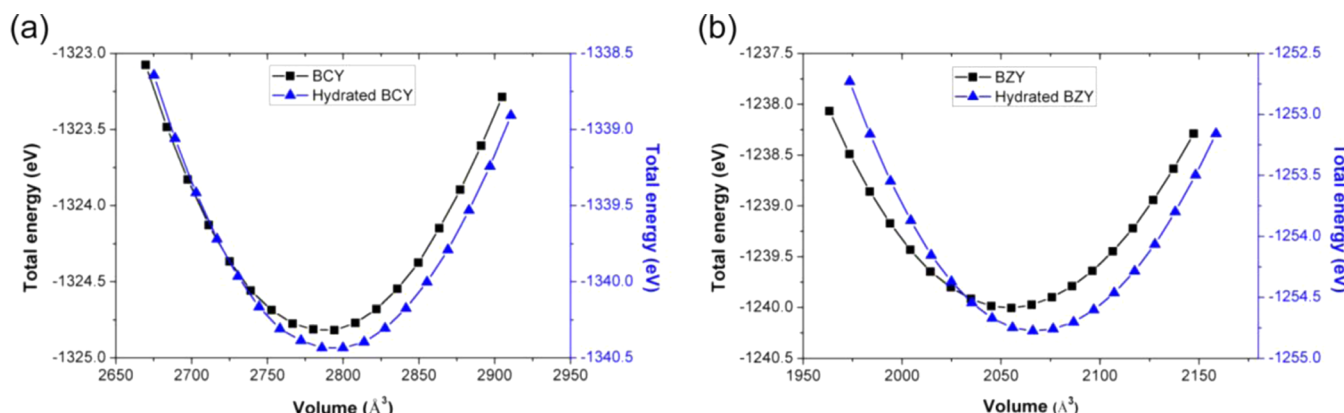


**Figure 8.** Total energy as a function of volume for (a) BCY and hydrated BCY and (b) BZY and hydrated BZY.

where  $E$  is the total energy,  $E_0$  and  $V_0$  are the equilibrium energy and volume, respectively,  $V$  is the deformed volume,  $B_0$  is the bulk modulus, and  $B_0'$  is the derivative of the bulk modulus with respect to energy. Based on the calculated equilibrium volume and volume change, the chemical

expansion upon hydration is obtained for BCY and BZY. Since the change in proton concentration is dictated by the simulations, this approach also enables determination of the CCE, i.e., the expansion normalized to the defect concentration change. As shown in Table 1, the simulations yield a

higher CCE at 0 K for BZY compared to that for BCY by more than a factor of 2, consistent with the experimental results. The simulated CCE for BZY is in good agreement with the experimentally measured value, while for BCY, the simulated CCE at 0 K is higher than the experimentally determined value at intermediate temperatures. It should be noted that the DFT simulations incorporate crystal chemical effects but not microstructural effects, so the qualitative agreement with the experimental trend suggests a crystal chemical contribution. Microstructural contributions were also studied and observed separately in the measurements, and those contributions, plus the change in crystal structure with temperature that is present for BCY but absent for BZY, may explain the difference in the measured vs simulated BCY CCE values.

The bulk moduli agree with the previous experimental and computational results.<sup>70–73</sup> In addition to the more stable configuration of two close Y dopants discussed here, both the BCY and BZY systems containing two distant Y dopants were also simulated for comparison. The structures are not shown here for brevity. Some of the results for this less stable configuration with distant Y dopants are included in Tables 1 and 2 in italics within round parentheses. These results are included here, as other reports have raised the possibility of experimental samples with distant Y dopant ions.

Additional selected results of the calculations are shown in Table 2. The zirconate exhibited a smaller effective oxygen vacancy volume than the cerate. The oxygen vacancy was also smaller than the oxide ion in the zirconate. The cerate exhibited a larger effective oxygen vacancy size, and in that case, the oxygen vacancy was found to have the same size as the oxide ion. Considering eq 1, during hydration (without simultaneous redox processes), an oxygen vacancy is replaced by a (OH) defect and an oxide ion is also replaced by a (OH) defect. Therefore, the effective size of the oxygen vacancy can play an important role in determining the extent of chemical strain or CCE.

#### 4. DISCUSSION

**4.1. Explanations for CCE Trends.** The experimental and computational results are in agreement that the hydration CCE decreases with decreasing Zr concentration in the Y-doped BaCeO<sub>3</sub>–BaZrO<sub>3</sub> solid solution across the temperature range studied. The results are consistent with our initial hypothesis that inducing distortions away from the perfect cubic perovskite structure would lower the CCE. We have also seen that there appear to be both crystal chemical and microstructural contributions to this trend related to symmetry from the DFT and *in situ* XRD results, respectively. However, the results have also revealed that there are multiple crystal chemical changes as the Ce/Zr ratio is altered, which go beyond our initial hypothesis about how symmetry/distortions might play a role in CCEs. To reiterate, we initially suggested that the distorted structures would accommodate compositional changes during hydration through changes in octahedral rotations/tilts, leading to some bonds lengthening and others shortening and an overall smaller volume change, compared to cubic structures. In this study, we found that many features changed when substituting Ce for Zr to lower the tolerance factor: symmetry, unit cell size, oxygen vacancy and oxide ion sizes, bulk moduli and bonding strengths, intra- vs interoctahedral hydrogen bonding, and method of proton incorporation (octahedral rotation vs bond bending). These factors are summarized in Table 3.

**Table 3. Summary of Trends in the Solid Solution**

feature	trend with increasing $x$ in BaCe <sub>0.9-x</sub> Zr <sub>x</sub> Y <sub>0.1</sub> O <sub>3-<math>\delta</math></sub> ( $0 \leq x \leq 0.9$ )
tolerance factor	↑
crystal symmetry	↑
unit cell volume	↓
B–O bond strength	↑ (Zr–O stronger than Ce–O)
bulk modulus	↑
method of proton incorporation	octahedral rotations → O–B–O bending
H-bonding type	interoctahedral → intraoctahedral
size ratio of oxygen vacancy: oxide ion	↓
CCE	↑

Factors that are perhaps somewhat extraneous to our initial hypothesis regarding symmetry effects include the unit cell volume, bond strength and related bulk modulus, and the relative size of the oxygen vacancy. Each of these may have contributed to the CCE trend independently of symmetry. Intuitively, one may expect that the insertion of a given amount of H<sub>2</sub>O into a smaller unit cell volume would give rise to a greater strain (since the volume change is normalized to the initial volume), assuming consistent effective sizes for (OH)<sub>0</sub>. The larger CCE for the smaller zirconates is consistent with that first-order expectation. Similarly, based on eq 1, one expects smaller oxygen vacancies in the dehydrated structure to give rise to larger chemical strains as the vacancies are filled by hydroxyl ions, again assuming a constant effective size of (OH)<sub>0</sub>. The relatively smaller oxygen vacancies in the zirconates are thus also consistent with their larger observed hydration CCEs. The expectation for the impact of bulk modulus or bond strength on CCEs is not so straightforward, but it is clear from the present work that not only crystal symmetry but also bond strengths play a role in determining how chemical stress from hydration is accommodated at the unit cell scale and which bond angles change.

However, some of these features in Table 3 may be related to each other. For example, Bjørheim et al.'s<sup>23</sup> phonon calculations showed a correlation between cubic symmetry, less negative (more favorable) hydration entropies, larger "chemical expansion coefficient of oxygen vacancies" (i.e., larger relative difference of the effective oxygen vacancy and oxide ion sizes), and thus larger hydration chemical expansion coefficients, albeit for limited compositions (cubic BaZrO<sub>3</sub> and BaSnO<sub>3</sub> vs orthorhombic BaCeO<sub>3</sub> and SrZrO<sub>3</sub>). They noted that the vibrational entropy contribution, particularly of the oxygen vacancies, dominated the compositional trend at finite temperatures, rather than the configurational entropy, which nonetheless has a more intuitive link to symmetry and unit cell volume via the variable positional degeneracy of oxygen vacancies and protons. Less negative entropies (more favorable hydration) correlated to less negative enthalpies (less favorable hydration), and the authors hypothesized that both of these properties ultimately relate to bonding strengths of oxide ions and protons. A monotonic trend of less negative hydration entropy vs increasing Zr content has also been observed for the solid solution in the present work.<sup>50</sup> Thus, indirect links between symmetry, relative oxygen vacancy size, bonding strengths, and hydration CCE are possible via the thermodynamics of hydration. On the other hand, by changing compositions, a number of factors in Table 3 can be decoupled

for more systematic studies and isolation of the effects of certain factors in future work.

**4.2. Temperature Effects.** Temperature-dependent CCEs have been observed for a number of perovskites undergoing redox-induced chemical expansion;<sup>44,74</sup> however, thermal trends for hydration CCEs have been less studied. Hydration CCEs increased with temperature across the conditions and composition range studied in the present work. The reasons for this trend remain relatively unexplored, but we note that in the cases of noncubic perovskites, their symmetry tends to increase with increasing temperature. This effect was demonstrated in the HTXRD results of the distorted  $\text{BaCe}_{0.9}\text{Y}_{0.1}\text{O}_{3-\delta}$  end member in the present work. As we have observed here a general correlation between increasing CCE and increasing symmetry, the temperature dependence of CCEs in  $\text{BaCe}_{0.9}\text{Y}_{0.1}\text{O}_{3-\delta}$  is consistent. For distorted  $\text{BaCe}_{0.9}\text{Y}_{0.1}\text{O}_{3-\delta}$ , even the isothermal chemical strains increased monotonically with increasing temperature, despite the isothermal proton concentration change peaking at an intermediate temperature for that composition. The opposite temperature dependence of chemical strain was apparent in cubic  $\text{BaZr}_{0.9}\text{Y}_{0.1}\text{O}_{3-\delta}$ , where isothermal hydration strain decreased with increasing temperature, consistent with the trend in its proton concentration change. Nonetheless, the cubic  $\text{BaZr}_{0.9}\text{Y}_{0.1}\text{O}_{3-\delta}$  composition did demonstrate a similar temperature dependence of the overall CCE, which cannot be explained by an increase of symmetry with increasing temperature. Instead, a potential contribution may come (to all compositions) from the tendency toward defect dissociation with increasing temperature; trapping of oxygen vacancies and/or protons near Y dopants will likely lessen during heating, leading to non-negligible and nonlinear modifications in the CCEs. The role of temperature-dependent hydration entropy contributions could also be considered.<sup>23</sup> A less likely contribution is the role of thermal expansion. We have observed here larger hydration CCEs for smaller (room-temperature) pseudocubic unit cell volumes when the volume is tailored by the Ce/Zr ratio. This correlation contrasts with the observed increasing CCE with increasing temperature, considering thermal expansion. However, the thermal expansion contribution to unit cell volume is relatively small compared to the effect of Ce/Zr exchange, and thus, temperature-dependent volume changes of the nonhydrated structures are perhaps negligible in influencing CCE. More work could be done to better clarify the underlying causes of temperature-dependent CCEs for these proton conductors. We included data from 680 °C in Figure 3b. This temperature was omitted from most of our result presentation, as we wished to ensure dominance of eq 1 as the hydration process being tested. We note that the trend of CCE vs composition begins to blur at 680 °C with all three lower Zr content compositions ( $0 \leq x \leq 0.6$ ) exhibiting similar CCEs. Temperature not only impacts crystal symmetry but also increases the populations of electronic defects. Thus, the redox chemical processes in eq 2 may start to come into play in determining CCEs at higher temperatures. Depending on the orbitals involved in hosting electronic defects and their spatial extent (delocalization), the electronic defects can play a role in determining the chemical strains under conditions enabling redox.<sup>27,61,75</sup>

**4.3. Microstructure and Dopant Distribution Effects on CCE Variability.** We minimized, as much as possible, variations in the microstructure when comparing between compositions in the solid solution using samples with a very

narrow distribution of relative densities and eliminating any isolated samples with microcracks. (In fact, a review of studies of thermal expansion on porous materials suggests that the role of varying porosity on expansion coefficients may be negligible.<sup>41</sup>) Nonetheless, through replicate analysis, we have noted variability in the hydration strains of different samples (having a broader microstructure and processing route range) of the anisotropically expanding cerate end member, as indicated by error bars on the plots. We also observed a difference in chemical strain between bulk and powder samples (Figure 8). These results are suggestive of an influence of microstructure (e.g., grain size), as hypothesized for lower-symmetry structures, on the CCEs. The implication is that, outside of single-crystal studies, a range of CCEs may be more descriptive of sintered, anisotropically expanding materials, with an as-yet-to-be-modeled dependence on microstructure. Furthermore, we suggest that variability in CCE for a given composition may also arise from the role of dopant distribution. The DFT simulations demonstrated that the lowest-energy configuration kept the Y dopants proximal to each other, with strong trapping of the protons by the dopants. However, the actual dopant distribution in samples may, in general, depend on the processing route, in particular, the sintering temperature and cooling rate after sintering, which may affect the “freezing-in” temperature of cation distributions. The trapping of defects by dopants may also lessen with increasing measurement temperature. It is worthwhile to remember that this dopant-defect distribution affected the CCEs and other parameters in the DFT simulations (Tables 1 and 2) and may also have this effect experimentally. In the present work, through the use of a consistent processing route, we endeavored to lessen variability in cation distribution among samples, but this effect should be considered, particularly when comparing among different studies and measurement temperatures.

## 5. CONCLUSIONS

Proton-conducting oxides enable the promising intermediate-temperature performance of protonic ceramic electrolysis/fuel cells, and their chemomechanical durability must be addressed to enable long device operating lifetimes. Isothermal macroscopic and axis-resolved chemical strains and associated quantified changes in proton changes in the  $\text{Ba-Ce}_{0.9-x}\text{Zr}_x\text{Y}_{0.1}\text{O}_{3-\delta}$  ( $0 \leq x \leq 0.9$ ) solid solution under equilibrium conditions were measured and simulated, leading to precise determination of hydration CCEs and their trends. In the intermediate-temperature range, the CCEs monotonically decrease with increasing Ce substitution for Zr. This trend is consistent with our initial hypothesis that the decreased perovskite crystal symmetry, relative to cubic  $Pm\bar{3}m$ , would lead to decreased CCEs. The results support this hypothesis; the tailoring of the tolerance factor does result in lower symmetries with increasing Ce content, and both crystal chemical and microstructural contributions expected from symmetry effects appear to be present according to DFT simulations and X-ray diffraction and dilatometry of powder vs bulk ceramic samples. Nonetheless, we observe that a number of other features systematically change across this solid solution, and some—like the effective relative oxygen vacancy size and unit cell volume—are also clearly consistent with the observed CCE trend. Future work that decouples these features and isolates their effects will be beneficial for developing broadly applicable design principles. At this stage,

we suggest that perovskite proton conductors with low symmetry, large oxygen vacancies, and large unit cells may exhibit low CCEs. For practical use, the Ce-rich compositions in the present study exhibit much lower hydration CCEs and lower chemical strains than the Zr-rich compositions in the conditions of this study and therefore likely greater macroscopic chemomechanical stability for implementation into intermediate-temperature electrochemical energy devices. On the other hand, it should be noted that the lower symmetry of the Ce-rich compositions also gives rise to more anisotropic chemical (and thermal) expansion, which may lead to enhanced grain boundary stresses between differently oriented grains. The CCE trend should also be considered in the broader context of properties that vary with the Zr:Ce ratio and tolerance factor in this solid solution, including stability in humid and CO<sub>2</sub>-rich environments,<sup>14</sup> basicity, sintering characteristics,<sup>10,11</sup> and transport behavior.<sup>12,13,15,16</sup>

## AUTHOR INFORMATION

### Corresponding Author

**Nicola H. Perry** — International Institute for Carbon-Neutral Energy Research, Kyushu University, Fukuoka 819-0395, Japan; Department of Materials Science and Engineering, University of Illinois at Urbana-Champaign, Urbana, Illinois 61801, United States; Materials Research Laboratory, University of Illinois at Urbana-Champaign, Urbana, Illinois 61801, United States;  [orcid.org/0000-0002-7207-2113](https://orcid.org/0000-0002-7207-2113); Email: [nhperry@illinois.edu](mailto:nhperry@illinois.edu)

### Authors

**Ting Chen** — International Institute for Carbon-Neutral Energy Research, Kyushu University, Fukuoka 819-0395, Japan; Department of Hydrogen Energy Systems, Kyushu University, Fukuoka 819-0395, Japan; Present Address: China Automotive Innovation Corporation Ltd., Building CAIC, No. 88 Shengli Road, Moling Street, Jiangning District, Nanjing, Jiangsu, 211100, China;  [orcid.org/0000-0002-9060-9834](https://orcid.org/0000-0002-9060-9834)

**Yuhang Jing** — Department of Mechanical Science and Engineering, University of Illinois at Urbana-Champaign, Urbana, Illinois 61801, United States; Present Address: Department of Astronautical Science and Mechanics, Harbin Institute of Technology, Harbin, Heilongjiang 150001, China.;  [orcid.org/0000-0001-5520-3866](https://orcid.org/0000-0001-5520-3866)

**Lawrence O. Anderson** — Department of Materials Science and Engineering, University of Illinois at Urbana-Champaign, Urbana, Illinois 61801, United States; Materials Research Laboratory, University of Illinois at Urbana-Champaign, Urbana, Illinois 61801, United States;  [orcid.org/0000-0003-0216-6170](https://orcid.org/0000-0003-0216-6170)

**Kwati Leonard** — International Institute for Carbon-Neutral Energy Research, Kyushu University, Fukuoka 819-0395, Japan

**Hiroshige Matsumoto** — International Institute for Carbon-Neutral Energy Research, Kyushu University, Fukuoka 819-0395, Japan

**Narayana Aluru** — Department of Mechanical Science and Engineering, University of Illinois at Urbana-Champaign, Urbana, Illinois 61801, United States; Present Address: Oden Institute for Computational Engineering and Sciences, Walker Department of Mechanical Engineering, The University of Texas at Austin, Austin,

Texas 78705, United States.;  [orcid.org/0000-0002-9622-7837](https://orcid.org/0000-0002-9622-7837)

Complete contact information is available at: <https://pubs.acs.org/10.1021/acs.jpcc.1c08334>

### Author Contributions

◆ T.C., Y.J., L.O.A., and K.L. contributed equally to this work. The manuscript was written through contributions of all authors. All authors have given approval to the final version of the manuscript.

### Notes

The authors declare no competing financial interest.

## ACKNOWLEDGMENTS

This work was supported financially by an NSF CAREER grant to N.H.P. (DMR-1945482) and initially by NSF grant no. 1545907 through a JSPS-NSF Partnership for International Research and Education (PIRE). The use of facilities and instrumentation was supported by NSF through the University of Illinois Materials Research Science and Engineering Center (DMR-1720633) and by the Materials Research Laboratory Central Research Facilities. The authors acknowledge support from the International Institute for Carbon Neutral Energy Research (WPI-I2CNER), sponsored by the Japanese Ministry of Education, Culture, Sports, Science and Technology. Computational work was performed using Blue Waters, which was provided by the University of Illinois and the National Center for Supercomputing Applications supported by NSF awards OCI-0725070 and ACI-1238993 and the state of Illinois.

## REFERENCES

- (1) Kreuer, K. D. Proton-Conducting Oxides. *Annu. Rev. Mater. Res.* **2003**, *33*, 333–359.
- (2) Iwahara, H.; Asakura, Y.; Katahira, K.; Tanaka, M. Prospect of Hydrogen Technology Using Proton-Conducting Ceramics. *Solid State Ionics* **2004**, *168*, 299–310.
- (3) Fabbri, E.; Bi, L.; Tanaka, H.; Pergolesi, D.; Traversa, E. Chemically Stable Pr and y Co-Doped Barium Zirconate Electrolytes with High Proton Conductivity for Intermediate-Temperature Solid Oxide Fuel Cells. *Adv. Funct. Mater.* **2011**, *21*, 158–166.
- (4) Murakami, T.; Hester, J. R.; Yashima, M. High Proton Conductivity in Ba<sub>2</sub>Er<sub>2</sub>Al<sub>2</sub>ZrO<sub>13</sub>, a Hexagonal Perovskite-Related Oxide with Intrinsically Oxygen-Deficient Layers. *J. Am. Chem. Soc.* **2020**, *142*, 11653–11657.
- (5) Rajendran, S.; Thangavel, N. K.; Ding, H.; Ding, Y.; Ding, D.; Reddy Arava, L. Tri-Doped BaCeO<sub>3</sub>-BaZrO<sub>3</sub> as a Chemically Stable Electrolyte with High Proton-Conductivity for Intermediate Temperature Solid Oxide Electrolysis Cells (SOECs). *ACS Appl. Mater. Interfaces* **2020**, *12*, 38275–38284.
- (6) Montaleone, D.; Mercadelli, E.; Escolástico, S.; Gondolini, A.; Serra, J. M.; Sanson, A. All-Ceramic Asymmetric Membranes with Superior Hydrogen Permeation. *J. Mater. Chem. A* **2018**, *6*, 15718–15727.
- (7) Yang, W.; Wang, L.; Li, Y.; Zhou, H.; He, Z.; Han, C.; Dai, L. An Easily Sintered, Chemically Stable Indium and Tin Co-Doped Barium Hafnate Electrolyte for Hydrogen Separation. *J. Alloys Compd.* **2021**, *868*, No. 159117.
- (8) Kreuer, K. D. On the Development of Proton Conducting Materials for Technological Applications. *Solid State Ionics* **1997**, *97*, 1–15.
- (9) Hamakawa, S.; Hibino, T.; Iwahara, H. Electrochemical Hydrogen Permeation in a Proton-Hole Mixed Conductor and Its Application to a Membrane Reactor. *J. Electrochem. Soc.* **1994**, *141*, No. 1720.

- (10) Park, J. S.; Lee, J. H.; Lee, H. W.; Kim, B. K. Low Temperature Sintering of BaZrO<sub>3</sub>-Based Proton Conductors for Intermediate Temperature Solid Oxide Fuel Cells. *Solid State Ionics* **2010**, *181*, 163–167.
- (11) Yun, D. S.; Kim, J.; Kim, S. J.; Lee, J. H.; Kim, J. N.; Yoon, H. C.; Yu, J. H.; Kwak, M.; Yoon, H.; Cho, Y.; et al. Structural and Electrochemical Properties of Dense Yttria-Doped Barium Zirconate Prepared by Solid-State Reactive Sintering. *Energies* **2018**, *11*, No. 3083.
- (12) Shirpour, M.; Merkle, R.; Lin, C. T.; Maier, J. Nonlinear Electrical Grain Boundary Properties in Proton Conducting Y-BaZrO<sub>3</sub> Supporting the Space Charge Depletion Model. *Phys. Chem. Chem. Phys.* **2012**, *14*, 730–740.
- (13) Han, D.; Liu, X.; Bjørheim, T. S.; Uda, T. Yttrium-Doped Barium Zirconate-Cerate Solid Solution as Proton Conducting Electrolyte: Why Higher Cerium Concentration Leads to Better Performance for Fuel Cells and Electrolysis Cells. *Adv. Energy Mater.* **2021**, *11*, No. 2003149.
- (14) Bhide, S. V.; Virkar, A. V. Stability of AB 1 / 2 ' B " 1 / 2 O 3 - Type Mixed Perovskite Proton Conductors. *J. Electrochem. Soc.* **1999**, *146*, No. 4386.
- (15) Lacz, A.; Grzesik, K.; Pasierb, P. Electrical Properties of BaCeO<sub>3</sub>-Based Composite Protonic Conductors. *J. Power Sources* **2015**, *279*, 80–87.
- (16) Hibino, T.; Iwahara, H. CO<sub>2</sub> Sensors Using BaCeO<sub>3</sub>-Based Ceramics. *Sens. Actuators, B* **1993**, *13*, 483–485.
- (17) Wallis, J.; Urban, L.; Grimmer, C.; Bodnar, W.; Zimmermann, R.; Ricote, S.; Weltmann, K. D.; Burkhardt, E.; Kruth, A. Structural and Electrical Properties of BaZr0.7Ce0.2Y0.1O3- $\delta$  Proton Conducting Ceramic Fabricated by Spark Plasma Sintering. *Solid State Ionics* **2020**, *345*, No. 115118.
- (18) Peng, J.; Li, H.; Lin, S. Study on Properties of BaZr0.7Ce0.2Y0.1O3- $\delta$  Ceramics Prepared by High-Pressure Sintering. *J. Ceram. Soc. Jpn.* **2020**, *128*, 62–65.
- (19) Poetzsch, D.; Merkle, R.; Maier, J. Proton Uptake in the H+-SOFC Cathode Material Ba<sub>0.5</sub>Sr<sub>0.5</sub>Fe<sub>0.8</sub>Zn<sub>0.2</sub>O<sub>3-d</sub>: Transition from Hydration to Hydrogenation with Increasing Oxygen Partial Pressure. *Faraday Discuss.* **2015**, *182*, 129–143.
- (20) Tsidilkovski, V. I.; Putilov, L. P. The Role of Deep Acceptor Levels in Hydration and Transport Processes in BaZr<sub>1-x</sub>Y<sub>x</sub>O<sub>3- $\delta$</sub>  and Related Materials. *J. Solid State Electrochem.* **2016**, *20*, 629–643.
- (21) Hoedl, M. F.; Gryaznov, D.; Merkle, R.; Kotomin, E. A.; Maier, J. Interdependence of Oxygenation and Hydration in Mixed-Conducting (Ba,Sr)FeO<sub>3- $\delta$</sub>  Perovskites Studied by Density Functional Theory. *J. Phys. Chem. C* **2020**, *124*, 11780–11789.
- (22) Poetzsch, D.; Merkle, R.; Maier, J. Stoichiometry Variation in Materials with Three Mobile Carriers—Thermodynamics and Transport Kinetics Exemplified for Protons, Oxygen Vacancies, and Holes. *Adv. Funct. Mater.* **2015**, *25*, 1542–1557.
- (23) Bjørheim, T. S.; Løken, A.; Haugsrud, R. On the Relationship between Chemical Expansion and Hydration Thermodynamics of Proton Conducting Perovskites. *J. Mater. Chem. A* **2016**, *4*, 5917–5924.
- (24) Torayev, A.; Sperrin, L.; Gomez, M. A.; Kattirtzi, J. A.; Merlet, C.; Grey, C. P. Local Distortions and Dynamics in Hydrated Y-Doped BaZrO<sub>3</sub>. *J. Phys. Chem. C* **2020**, *124*, 16689–16701.
- (25) Chen, X.; Grande, T. Anisotropic Chemical Expansion of La<sub>1-x</sub>Sr<sub>x</sub>CoO<sub>3- $\delta$</sub> . *Chem. Mater.* **2013**, *25*, 927–934.
- (26) Chen, X.; Grande, T. Anisotropic and Nonlinear Thermal and Chemical Expansion of La<sub>1-x</sub>Sr<sub>x</sub>FeO<sub>3- $\delta$</sub>  ( $x = 0.3, 0.4, 0.5$ ) Perovskite Materials. *Chem. Mater.* **2013**, *25*, 3296–3306.
- (27) Perry, N. H.; Bishop, S. R.; Tuller, H. L. Tailoring Chemical Expansion by Controlling Charge Localization: In Situ X-Ray Diffraction and Dilatometric Study of (La,Sr)(Ga,Ni)O<sub>3- $\delta$</sub>  Perovskite. *J. Mater. Chem. A* **2014**, *2*, 18906–18916.
- (28) Brett, D. J. L.; Atkinson, A.; Brandon, N. P.; Skinner, S. J. Intermediate Temperature Solid Oxide Fuel Cells. *Chem. Soc. Rev.* **2008**, *37*, 1568–1578.
- (29) Han, D.; Shinoda, K.; Sato, S.; Majima, M.; Uda, T. Correlation between Electroconductive and Structural Properties of Proton Conductive Acceptor-Doped Barium Zirconate. *J. Mater. Chem. A* **2015**, *3*, 1243–1250.
- (30) Kinyanjui, F. G.; Norberg, S. T.; Ahmed, I.; Eriksson, S. G.; Hull, S. In-Situ Conductivity and Hydration Studies of Proton Conductors Using Neutron Powder Diffraction. *Solid State Ionics* **2012**, *225*, 312–316.
- (31) Andersson, A. K. E. E.; Selbach, S. M.; Knee, C. S.; Grande, T. Chemical Expansion Due to Hydration of Proton-Conducting Perovskite Oxide Ceramics. *J. Am. Ceram. Soc.* **2014**, *97*, 2654–2661.
- (32) Han, D.; Hatada, N.; Uda, T.; Koc, R. Chemical Expansion of Yttrium-Doped Barium Zirconate and Correlation with Proton Concentration and Conductivity. *J. Am. Ceram. Soc.* **2016**, *99*, 3745–3753.
- (33) Mather, G. C.; Heras-Juaristi, G.; Ritter, C.; Fuentes, R. O.; Chinellatto, A. L.; Pérez-Coll, D.; Amador, U. Phase Transitions, Chemical Expansion, and Deuteron Sites in the BaZr0.7-Ce0.2Y0.1O3- $\delta$  Proton Conductor. *Chem. Mater.* **2016**, *28*, 4292–4299.
- (34) Ricote, S.; Hudish, G.; O'Brien, J. R.; Perry, N. H. Non Stoichiometry and Lattice Expansion of BaZr0.9Dy0.1O3- $\delta$  in Oxidizing Atmospheres. *Solid State Ionics* **2019**, *330*, 33–39.
- (35) Tarutina, L. R.; Vdovin, G. K.; Lyagaeva, J. G.; Medvedev, D. A. BaCe0.7-XZr0.2Y0.1FeO3- $\delta$  Derived from Proton-Conducting Electrolytes: A Way of Designing Chemically Compatible Cathodes for Solid Oxide Fuel Cells. *J. Alloys Compd.* **2020**, *831*, No. 154895.
- (36) Sosnowska, I.; Przenioslo, R.; Schäfer, W.; Kockelmann, W.; Hempelmann, R.; Wysocki, K. Possible Deuterium Positions in the High-Temperature Deuterated Proton Conductor Ba<sub>3</sub>Ca<sub>1+y</sub>Nb<sub>2-y</sub>YO<sub>9- $\delta$</sub>  Studied by Neutron and X-Ray Powder Diffraction. *J. Alloys Compd.* **2001**, *328*, 226–230.
- (37) Hudish, G.; Manerbino, A.; Coors, W. G.; Ricote, S. Chemical Expansion in BaZr0.9-xCexY0.1O3- $\delta$  ( $x = 0$  and  $0.2$ ) upon Hydration Determined by High-Temperature X-Ray Diffraction. *J. Am. Ceram. Soc.* **2018**, *101*, 1298–1309.
- (38) Sereda, V. V.; Tsvetkov, D. S.; Malyshevkin, D. A.; Ivanov, I. L.; Sednev-Lugovets, A. L.; Zuev, A. Y. Hydration-Induced Chemical Expansion of BaCa(1+y)/3Nb(2-y)/3O3- $\delta$ •xH<sub>2</sub>O (BCN) and Other Proton-Conducting Perovskite Oxides. *Solid State Ionics* **2020**, *358*, No. 115516.
- (39) Fujisaki, T.; Staykov, A. T.; Jing, Y.; Leonard, K.; Aluru, N. R.; Matsumoto, H. Understanding the Effect of Ce and Zr on Chemical Expansion in Yttrium Doped Strontium Cerate and Zirconate by High Temperature X-Ray Analysis and Density Functional Theory. *Solid State Ionics* **2019**, *333*, 1–8.
- (40) Tsidilkovski, V.; Kuzmin, A.; Putilov, L.; Balakireva, V. H/D Isotope Effect for Hydrogen Solubility in BaZr0.9Y0.1O3- $\delta$ : Chemical Expansion Studies. *Solid State Ionics* **2017**, *301*, 170–175.
- (41) Løken, A.; Ricote, S.; Wachowski, S. Thermal and Chemical Expansion in Proton Ceramic Electrolytes and Compatible Electrodes. *Crystals* **2018**, *8*, No. 365.
- (42) Yamaguchi, S.; Yamada, N.; et al. Thermal Lattice Expansion Behavior of Yb-Doped BaCeO<sub>3</sub>. *Solid State Ionics* **2003**, *162*–163, 23–29.
- (43) Anderson, L. O.; Bin Yong, A. X.; Ertekin, E.; Perry, N. H. Toward Zero-Strain Mixed Conductors: Anomalously Low Redox Coefficients of Chemical Expansion in Praseodymium-Oxide Perovskites. *Chem. Mater.* **2021**, *33*, 8378–8393.
- (44) Kim, C. S.; Perry, N. H.; Bishop, S. R.; Tuller, H. L. Electro-Chemo-Mechanical Studies of Perovskite-Structured Mixed Ionic-Electronic Conducting SrSn<sub>1-x</sub>FeO<sub>3-x/2+ $\delta$</sub>  Part III: Thermal and Chemical Expansion. *J. Electroceram.* **2018**, *40*, 332–337.
- (45) Grande, T.; Tolchard, J. R.; Selbach, S. M. Anisotropic Thermal and Chemical Expansion in Sr-Substituted LaMnO<sub>3+ $\delta$</sub> : Implications for Chemical Strain Relaxation. *Chem. Mater.* **2012**, *24*, 338–345.
- (46) Leonard, K.; Lee, Y. S.; Okuyama, Y.; Miyazaki, K.; Matsumoto, H. Influence of Dopant Levels on the Hydration Properties of SZCY

- and BZCY Proton Conducting Ceramics for Hydrogen Production. *Int. J. Hydrogen Energy* **2017**, *42*, 3926–3937.
- (47) Shannon, R. D. Revised Effective Ionic Radii and Systematic Studies of Interatomic Distances in Halides and Chalcogenides. *Acta Crystallogr., Sect. A: Cryst. Phys., Diffraction, Theor. Gen. Crystallogr.* **1976**, *32*, 751–767.
- (48) Goldschmidt, V. M. The Laws of Crystal Chemistry. *Naturwissenschaften* **1926**, *14*, 477–485.
- (49) He, T.; Kreuer, K. D.; Baikov, Y. M.; Maier, J. Impedance Spectroscopic Study of Thermodynamics and Kinetics of a Gd-Doped BaCeO<sub>3</sub> Single Crystal. *Solid State Ionics* **1997**, *95*, 301–308.
- (50) Ricote, S.; Bonanos, N.; Caboche, G. Water Vapour Solubility and Conductivity Study of the Proton Conductor BaCe(0.9 – x)ZrxY0.1O<sub>3</sub> – δ. *Solid State Ionics* **2009**, *180*, 990–997.
- (51) Kresse, G.; Furthmüller, J. Efficiency of Ab-Initio Total Energy Calculations for Metals and Semiconductors Using a Plane-Wave Basis Set. *Comput. Mater. Sci.* **1996**, *6*, 15–50.
- (52) Kresse, G.; Joubert, D. From Ultrasoft Pseudopotentials to the Projector Augmented-Wave Method. *Phys. Rev. B* **1999**, *59*, No. 1758.
- (53) Kresse, G.; Furthmüller, J. Efficient Iterative Schemes for Ab Initio Total-Energy Calculations Using a Plane-Wave Basis Set. *Phys. Rev. B* **1996**, *54*, No. 11169.
- (54) Perdew, J. P.; Burke, K.; Ernzerhof, M. Generalized Gradient Approximation Made Simple. *Phys. Rev. Lett.* **1996**, *77*, No. 3865.
- (55) Swift, M.; Janotti, A.; Van De Walle, C. G. Small Polarons and Point Defects in Barium Cerate. *Phys. Rev. B* **2015**, *92*, No. 214114.
- (56) Levin, I.; Amos, T. G.; Bell, S. M.; Farber, L.; Vanderah, T. A.; Roth, R. S.; Toby, B. H. Phase Equilibria, Crystal Structures, and Dielectric Anomaly in the BaZrO<sub>3</sub>-CaZrO<sub>3</sub> System. *J. Solid State Chem.* **2003**, *175*, 170–181.
- (57) Kreuer, K. D.; Schönherr, E.; Maier, J. Proton and Oxygen Diffusion in BaCeO<sub>3</sub> Based Compounds: A Combined Thermal Gravimetric Analysis and Conductivity Study. *Solid State Ionics* **1994**, *70*, 278–284.
- (58) Kim, G. R.; Seo, H. H.; Jo, J. M.; Shin, E. C.; Yu, J. H.; Lee, J. S. Moving Boundary Diffusion Problem for Hydration Kinetics Evidenced in Non-Monotonic Conductivity Relaxations of Proton Conducting Perovskites. *Solid State Ionics* **2015**, *272*, 60–73.
- (59) Samborski, S.; Sadowski, T. Dynamic Fracture Toughness of Porous Ceramics. *J. Am. Ceram. Soc.* **2010**, *93*, 3607–3609.
- (60) Rice, R. W. Grain Size and Porosity Dependence of Ceramic Fracture Energy and Toughness at 22 °C. *J. Mater. Sci.* **1996**, *31*, 1969–1983.
- (61) Perry, N. H.; Kim, J. J.; Bishop, S. R.; Tuller, H. L. Strongly Coupled Thermal and Chemical Expansion in the Perovskite Oxide System Sr(Ti,Fe)O<sub>3</sub>-α. *J. Mater. Chem. A* **2015**, *3*, 3602–3611.
- (62) Omar, S.; Nino, J. C. Consistency in the Chemical Expansion of Fluorites: A Thermal Revision of the Doped Ceria. *Acta Mater.* **2013**, *61*, 5406–5413.
- (63) Takahashi, H.; Yashima, I.; Amezawa, K.; Eguchi, K.; Matsumoto, H.; Takamura, H.; Yamaguchi, S. First-Principles Calculations for the Energetics of the Hydration Reaction of Acceptor-Doped BaZrO<sub>3</sub>. *Chem. Mater.* **2017**, *29*, 1518–1526.
- (64) Yamazaki, Y.; Blanc, F.; Okuyama, Y.; Buannic, L.; Lucio-Vega, J. C.; Grey, C. P.; Haile, S. M. Proton Trapping in Yttrium-Doped Barium Zirconate. *Nat. Mater.* **2013**, *12*, 647–651.
- (65) Bjørheim, T. S.; Kuwabara, A.; Ahmed, I.; Haugsrud, R.; Stølen, S.; Norby, T. A Combined Conductivity and DFT Study of Protons in PbZrO<sub>3</sub> and Alkaline Earth Zirconate Perovskites. *Solid State Ionics* **2010**, *181*, 130–137.
- (66) Kreuer, K. D. Aspects of the Formation and Mobility of Protonic Charge Carriers and the Stability of Perovskite-Type Oxides. *Solid State Ionics* **1999**, *125*, 285–302.
- (67) Hermet, J.; Bottin, F.; Dezanneau, G.; Geneste, G. Thermodynamics of Hydration and Oxidation in the Proton Conductor Gd-Doped Barium Cerate from Density Functional Theory Calculations. *Phys. Rev. B* **2012**, *85*, No. 205137.
- (68) Birch, F. Finite Elastic Strain of Cubic Crystals. *Phys. Rev.* **1947**, *71*, No. 809.
- (69) Murnaghan, F. D. The Compressibility of Media under Extreme Pressures. *Proc. Natl. Acad. Sci. U.S.A.* **1944**, *30*, No. 244.
- (70) Zhang, J.; Zhao, Y.; Xu, H.; Li, B.; Weidner, D. J.; Navrotsky, A. Elastic Properties of Yttrium-Doped BaCeO<sub>3</sub> Perovskite. *Appl. Phys. Lett.* **2007**, *90*, No. 161903.
- (71) Yamanaka, S.; Fujikane, M.; Hamaguchi, T.; Muta, H.; Oyama, T.; Matsuda, T.; Kobayashi, S. I.; Kuroski, K. Thermophysical Properties of BaZrO<sub>3</sub> and BaCeO<sub>3</sub>. *J. Alloys Compd.* **2003**, *359*, 109–113.
- (72) Gorecka, K. C.; Park, E. T.; Koritala, R. E.; Cuber, M. M.; Pascual, E. A.; Chen, N.; De Arellano-López, A. R.; Routbort, J. L. Thermomechanical Response of Polycrystalline BaZrO<sub>3</sub>. *Phys. C* **1998**, *309*, 245–250.
- (73) Malagoli, M.; Liu, M. L.; Park, H. C.; Bongiorno, A. Protons Crossing Triple Phase Boundaries Based on a Metal Catalyst, Pd or Ni, and Barium Zirconate. *Phys. Chem. Chem. Phys.* **2013**, *15*, 12525–12529.
- (74) Perry, N. H.; Marrocchelli, D.; Bishop, S. R.; Tuller, H. L. Understanding and Controlling Chemo-Mechanical Coupling in Perovskite Oxides. *ECS Trans.* **2016**, *72*, No. 1.
- (75) Marrocchelli, D.; Bishop, S. R.; Tuller, H. L.; Watson, G. W.; Yildiz, B. Charge Localization Increases Chemical Expansion in Cerium-Based Oxides. *Phys. Chem. Chem. Phys.* **2012**, *14*, 12070–12074.